A Dive into the Electrodeposition Kinetics and Mechanisms in Nonaqueous Magnesium Electrolytes.

Journal:	*Journal of The Electrochemical Society*
Manuscript ID	Draft
Manuscript Type:	Research Paper
Date Submitted by the Author:	n/a
Complete List of Authors:	Sa, Niya; Argonne National Laboratory, Chemical Sciences and Engineering Division Asselin, Genevieve ; University of Massachusetts Boston Yang, Zicheng; University of Massachusetts Boston
Keywords:	Electrode Kinetics, Electroanalytical Electrochemistry, Electrodeposition, Energy Storage, Batteries

A Dive into the Electrodeposition Kinetics and Mechanisms in Nonaqueous Magnesium Electrolytes

Genevieve Asselin[a], Zicheng Yang[a], Niya Sa[a]*

[a] Department of Chemistry, University of Massachusetts Boston, 100 Morrissey Boulevard, Boston, MA 02125

ABSTRACT

The fundamental complexity of the divalent chemistry of Mg^{2+} necessitates in-situ isolation of the intertwined electron transfer and chemical steps during reversible electrochemical deposition of Mg. To clarify the impact of the solution environment of Mg^{2+} on the electron transfer mechanism an All Phenyl Complex (APC) and a $Mg(TFSI)_2$ electrolyte were examined electrochemically *in-situ* and supported with simulation. Key mechanistic steps were found to take place in both the APC and Mg(TFSI)2 electrolyte including a rate-limiting Mg^{2+} desolvation/adsorption step and the subsequent occurrence of two independent electron transfers. The first electron transfer forms a newly electrochemically captured transient $Mg^{\bullet+}$ relevant radical intermediate and the second electron transfer reaction forms plated Mg0 metal. During dissolution, an adsorbed $Mg^{\bullet+}$ relevant radical intermediate is proposed to exist at the disk electrode in contrast to the mobile $Mg^{\bullet+}$ relevant intermediate observed during Mg^{2+} reduction. APC demonstrated a more facile redox mechanism, but it is clear that the Mg^{2+} species, both chloride and TFSI- coordinated magnesium electrolytes, undergo the same electron transfer mechanism of a two-step one electron process with preceding chemical steps despite radically different solvation environments, giving broad insight into the underlying working mechanism of magnesium electrolytes for rechargeable battery applications.

INTRODUCTION

Magnesium ion battery (MIB) chemistries have emerged as interesting alternatives to address the inherent limitations of Lithium-ion battery chemistry. If high reversibility can be achieved, MIBs introduce the possibility of enabling the magnesium metal anodes for high energy density batteries with better safety and lower material cost, among other advantages.[1–5] Despite promise, glaring knowledge gaps remain about charge transfer processes, hindering progress towards electrochemically stable and reversible electrolytes.[6] Even the fundamental question of whether magnesium undergoes two separate electron transfers, or a single two-electron transfer during plating and stripping processes has remained largely unresolved.[3,7–12] Uncertainties in solution structure and its role in electrochemistry have persisted despite that cation coordination environment can significantly impact electrochemical properties such as redox potentials, energies of solvation/desolvation, as well as possible intermediate formation. This fundamental relationship between the coordination structure and electrochemical activity is critical to build a clear picture of the process of charge transfer during redox events.

All-phenyl complex (APC) electrolytes offer noteworthy advantages including exceptional reversibility and good compatibility with Mg metal anodes.[4,13–15] Non-halogenated electrolytes on the other hand are touted as an essential step forward in MIB development to push the limits of electrochemical stability windows, enhance compatibility of cell components and cathode materials, and reduce sensitivity to water and oxygen.[14,16,17] Magnesium bis(trifluoromethylsulfonyl)imide ($Mg(TFSI)_2$) electrolytes have been of particular interest due to $TFSI^-$'s electron delocalization, weak coordination with Mg^{2+}, good anodic stability, increased compatibility with cathode materials, and simplicity of electrolyte formulation.[6,17,18] Sa's group reported on a new Mg electrolyte (subsequently referred to as *nh*Mg-DMA where *nh* refers to "non-halogen" in reference to its lack of corrosive chloride) with a neutrally charged $TFSI^-$-coordinated electrochemically active Mg^{2+} in tetrahydrofuran utilizing dimethylamine (DMA) as a critical cosolvent to enhance solubilization and coulombic efficiency due to its participation in an outer solvation shell.[17,19,20] Solution structure has proven to play a significant role in desolvation, ion transport, and electrochemical stability in rechargeable systems.[9,21] Intermediate formation certainly is impacted

as, for example, ion pairing, common in multivalent electrolytes, can considerably change the stability of chemical species in solution.[22,23] Grignard-type electrolytes give rise to a wide variety of Mg species in solution to form a complex solution structure whereas $Mg(TFSI)_2$ electrolytes form a simple solution structure with one dominant Mg species.[3,4,24,25] It is not clear, however, whether solvation structure determines the electron transfer mechanism of the Mg cation itself, or perhaps solvent and anion stability bear the brunt of mechanistic changes. It is therefore worth directly asking whether electron transfer mechanisms of Mg^{2+} reduction and Mg^0 oxidation significantly differ between electrolyte compositions.

Complex electrochemical responses often arise from mechanisms with coupled electron transfer and chemical steps. Previous studies have postulated that chemical steps may accompany electron transfer steps in Mg electrolyte systems.[11,12,26–28] Benmayza et al. suggested a mechanism for APC in which a disproportionation of the well-known $[Mg_2(\mu\text{-}Cl)_3 \cdot 6THF]^+$ results in $MgCl_2 \cdot 4THF$ and the electrochemically active $(MgCl \cdot 5THF)^+$ species.[26] Ta et al. built upon these findings and concluded that Mg plating proceeds with a chemical-electrochemical (CE) mechanism in which the disproportionation step to create $(MgCl \cdot 5THF)^+$ accounted for their observation of a scan rate-dependent chemical step prior to electron transfer.[11] Ha et al. also proposed possibility of the adsorbed Mg^{2+} complexes due to pre-deposition compressive stress in three organohaloaluminate electrolytes as well as a mixed cation Mg borohydride electrolyte.[12] However, a comprehensive understanding of the working mechanism and kinetics of magnesium plating and stripping processes is imperative to realize Mg metal anodes and is crucial to build a foundation for novel electrolyte innovation. As such, further progress in magnesium electrolyte development is functionally reduced to a guess and check strategy if the mechanisms of electron transfer, kinetics, and intermediate formation of existing systems are not well understood. In this work, the hydrodynamic effect and kinetics of electron transfer of *nh*Mg-DMA and APC were explored in-situ and findings suggest a multi-step electron transfer mechanism where Mg^{2+} first undergoes a kinetically sluggish adsorption and desolvation step before a stepwise reduction to $Mg^{\bullet+}$ and then to Mg^0, confirming a CE mechanism where a chemical step takes place before the electron transfer reaction. Upon dissolution, a CE mechanism is also proposed with the formation of an adsorbed $Mg^{\bullet+}$-relevant radical that is rapidly oxidized further to Mg^{2+}. Despite significant differences in solvation and speciation, APC and *nh*Mg-DMA demonstrate striking similarities in their stepwise electron transfer mechanisms bearing differences in kinetics of the $Mg^{\bullet+}$-relevant radical.

EXPERIMENTAL

Electrolyte preparation. All electrolyte preparation and electrochemical characterizations were conducted in an argon-filled glove box (Vacuum Technology Inc.) with H_2O and O_2 level under 0.1 ppm. To make 0.3 M APC electrolyte, THF (Aldrich, Anhydrous 99.5%) was dried over molecular sieves (Aldrich, 3 Å beads) and chilled before use. Aluminum chloride (99.999%, Sigma Aldrich) was dried overnight under vacuum at room temperature. Chilled THF was added to $AlCl_3$ dropwise and mixed until clear. Once uniform, phenylmagnesium chloride (2.0 M in THF, Sigma Aldrich) was added and the electrolyte mixed overnight to form a clear solution with a 2:1 PhMgCl to $AlCl_3$ ratio. Magnesium (II) bis(trifluoromethanesulfonyl)imide (Solvionic, 99.9%) was dried overnight at 180 °C and dissolved in 2.0 M dimethylamine in THF (Sigma Aldrich, 99.5% anhydrous) (dried over molecular sieves) and mixed until clear to prepare 0.4 M $Mg(TFSI)_2$ in 2.0 M DMA in THF.

Rotating Ring Disk Electrode (RRDE) Setup. A RRDE from Pine Research was used, with a platinum ring electrode (inner diameter 6.5 mm, outer diameter 7.5 mm) with a platinum disk insert (5 mm diameter) polished before use. Magnesium metal ribbons were scraped and used as counter and reference electrodes. Electrochemistry was carried out using a multichannel potentiostat (Parstat MC 1000, Princeton Instruments) in a bipotentiostat configuration by scanning the disk electrode at a scan rate of 0.05 V/s while biasing the ring electrode at an oxidizing potential. Cyclic voltammetry (CV) of each electrolyte with no rotation are presented in **Figure S1a** and **b** and multiple RRDE cycles of each electrolyte in **S1c** and **d**. Electrochemistry was conducted in duplicate.

The current observed at the disk electrode is described by the Levich equation. According to the Levich equation (**equation 1**), for mass transport limited reactions, a higher rotation speed theoretically results in elevated current due to the increased mass transport from induced laminar flow at the disk electrode and a reduced diffusion layer thickness.[29]

$$i_D = 0.201nFAD^{2/3}v^{-1/6}\omega^{1/2}C \qquad \text{(eq. 1)}$$

where n is the number of electrons, F is faraday's constant, A is the electrode area (cm^2), D is the diffusion coefficient (cm/s), ν is the kinematic viscosity (cm^2/s), ω is the rotation speed (RPM), and C is the concentration (mol/cm^3). The current is dependent on rotation speed in an ideal system with fast kinetics and a one-electron transfer. The highest current was used as the Levich current in the absence of a limiting current.

The current equation for the ring electrode is likewise described in **equation 2**:[29]

$$i_R = 0.201nF\pi(r_2^3 - r_3^3)^{2/3}D^{2/3}\nu^{-1/6}C\omega^{1/2} \quad \text{(eq. 2)}$$

The Koutecky Levich equation is more useful in the study of non-mass transport-controlled reactions by allowing the extraction of current contributed by the kinetics of the reaction in the following **equation 3**:[29]

$$\frac{1}{i} = \frac{1}{i_k} + \left(\frac{1}{0.201nFAD^{2/3}\nu^{-1/6}C}\right)\omega^{-1/2} \quad \text{(eq. 3)}$$

where i_k is the kinetic current.

Attenuated Total Reflectance Fourier Transfer Infrared Spectroscopy (ATR-FTIR) Measurement. Ex-situ ATR-FTIR spectra were acquired for pristine electrolyte, electrolyte after five CV cycles, and electrolyte after 50 CV cycles using a Nicolet iS50 FTIR with attenuated total reflectance mode. A total of 32 scans were collected at a spectral resolution of 4 cm^{-1} between 4000 cm^{-1} and 400 cm^{-1}. The CV was performed for APC electrolyte at 0.05 V/s between -0.5 to 0.75 V vs Mg. CV was performed for *nh*Mg-DMA electrolyte from -1.0 V to 2.2 V vs Mg at a scan rate of 0.05 V/sec. OMNIC software was used for data acquisition.

Finite Element COMSOL Simulation. A two-dimensional finite element simulation model was built and solved by COMSOL Multiphysics 6.1 (COMSOL Inc. Burlington, MA, U.S.A.) The Butler-Volmer equation is used to describe the kinetic current in **equation 4**:

$$i = j_{0AB}(\mathrm{C}_A(0,t)\exp\left(\frac{\alpha F}{RT}\eta\right) - \mathrm{C}_B(0,t)\exp\left(-\frac{(1-\alpha)F}{RT}\eta\right) \quad \text{(eq. 4)}$$

Where i is the current density, j_{0AB} is the exchange current density of the reaction between species A and B, $\mathrm{C}_A(0,t)$ is the concentration of species A at a given position and time, α is the charge transfer coefficient, F is Faraday's constant, R is the gas constant, T is the temperature, η is overpotential, and $\mathrm{C}_B(0,t)$ is the concentration of species B at a given position and time.

The Nernst Planck equation was applied to determine the mass transport shown in **equation 5**. Ion flux is contributed from diffusion and convection with migration omitted in **equation 6**. The concentration variable at the electrode surface is calculated by the electrochemical kinetics from Butler-Volmer coupled with mass transport in bulk solution from Nernst Planck.

$$\frac{\partial c}{\partial t} + \nabla \cdot \boldsymbol{J} = 0 \quad \text{(eq.5)}$$

$$\boldsymbol{J} = -D\nabla \mathrm{c} + \mathrm{c}\mathbf{v} \quad \text{(eq.6)}$$

Where the ∇c is the concentration gradient, $\boldsymbol{J}$ is the flux, $\nabla \cdot \boldsymbol{J}$ is the flux divergence, D is the diffusion coefficient, and $\boldsymbol{v}$ is the flow velocity.

The convective hydrodynamic flow pattern of the cross-section of the cell observed between the center of the disk and the outer bulk edge was assumed to simply follow a circular flow pattern (**equation 7**), solving for the z and r axis velocity vectors:

$$(z - 0.1)^2 + r^2 = 0.1^2 \quad \text{(eq. 7)}$$

Where the center is at (0.1, 0) meters and z and r are the flow velocity vectors along the z axis and r axis. The z and r vectors are multiplied by the rotation speed and radius.

The reaction domain size was defined as 0.2 by 0.2 m. The disk and ring electrode widths were defined as 5 mm and 1.5 mm respectively (dimensional definition is shown in **Figure S2**). Initial bulk concentration was 1×10^{-7} $mmol/m^3$. CV was applied at the disk electrode in a potential window of -1.0 V to 1.0 V at a scan rate of 0.1 V/s. In the simulation model, a first single electron transfer redox reaction, $A + e^- \rightarrow B$ has an equilibrium potential of 0.1 V (generically representing $Mg^{2+} \rightarrow Mg^+$ in experimental studies). At the ring electrode, a constant potential of 1.0 V is biased for the reverse oxidation reaction, $B - e^- \rightarrow A$, (representing $Mg^+ \rightarrow Mg^{2+}$ in experiments). Another third redox reaction, defined as $C + e^- \rightarrow D$ has an equilibrium potential 0.5 V (representing $TFSI^- \rightarrow TFSI^{2-}$ in experiments).

RESULTS AND DISCUSSION

Possible reactions in *nh*Mg-DMA:

Reduction reactions at the disk electrode:

$TFSI^- + e^- \rightarrow TFSI^{\bullet 2-}$ ($1d_{red}$)*

$Mg^{2+} + e^- \rightarrow Mg^{\bullet +}$ ($2d_{red}$)*

$Mg^{\bullet +} + e^- \rightarrow Mg^0$ ($3d_{red}$)*

$Mg^{2+} + 2e^- \rightarrow Mg^0$ ($4d_{red}$)

Oxidation reactions at the disk electrode:

$Mg^{\bullet +} - e^- \rightarrow Mg^{2+}$ ($2d_{ox}$)

$Mg^0 - e^- \rightarrow Mg^{\bullet +}$ ($3d_{ox}$)

$Mg^0 - 2e^- \rightarrow Mg^{2+}$ ($4d_{ox}$)*

$DMA - e^- \rightarrow decomposed\ DMA$ ($5d_{ox}$)

Oxidation reactions at the ring:

$TFSI^{\bullet 2-} - e^- \rightarrow TFSI^-$ ($1r_{ox}$)*

$Mg^{\bullet +} - e^- \rightarrow Mg^{2+}$ ($2r_{ox}$)*

The listed proposed reactions are identified according to two standards including (1) possible reactions based on the chemical species in the electrolyte systems, and (2) redox reactions identified by their electrochemical response from both disk and ring current responses. The latter is identified by an asterisk (*) in the reaction list.

Experimentally probed electron transfer during Mg plating in nhMg-DMA. To characterize the stepwise electron transfer mechanisms of Mg plating and stripping, RRDE studies were conducted to allow separation between simultaneous chemical and redox events. **Figure 1a** shows the collection of the disk (lower panel) and ring currents (upper panel) from a 0.4 M $Mg(TFSI)_2$ electrolyte with 2.0 M dimethylamine as a cosolvent in THF (subsequently referred to as *nh*Mg-DMA). Voltage is shown on the lower panel x axis, corresponding to time on the upper panel x axis. Either *d* or *r* is used to designate reactions occurring at the ring or the disk and subscripts $_{red}$ and $_{ox}$ are used to specify a reduction or an oxidation reaction. A diffusion-limited current plateau emerged (200 s to 230 s) attributed to $TFSI^-$ reduction (reaction $1d_{red}$), as the disk electrode voltage was scanned from 1.0 V to -0.5 V, resulting in -18 μA at 0 RPM and almost -200 μA at 1000 RPM in **Figure 1a**.[30] A corresponding oxidative limiting current plateau ($1r_{ox}$) of 2.5 μA at 0 RPM and 14.7 μA at 1000 RPM was observed at the ring electrode, biased at 2.0 V (area enlarged in **Figure 1b**). Simultaneous limiting currents at the ring and disk electrodes indicate that the $TFSI^-$ reduction process at the disk either is at least partially reversible as a meta-stable dianion,[31] or it produces an oxidizable degradation product.[9,29–32] Most reported research largely supports the splitting of the C-S bond, releasing CF^{3-}, or splitting the S-N bonds of the $TFSI^-$ to produce reduction products.[9,31,32] ATR-FTIR shows no significant changes in the electrolyte composition over 50 cycles (**Figure S3**). Calculations of the isolated $TFSI^-$ anion reduction potential predict that reduction occurs lower than 0.25 V vs Mg.[30,33] The formation of ionic aggregates (AGGs) in the presence of cationic species, however, significantly compromises the anion stability and increases the reduction potential of $TFSI^-$, according to DFT calculations.[9,31] *nh*Mg-DMA is known to form AGGs in solution[9] that here consequently drive the reduction of $TFSI^-$ up to 1.0 V vs Mg.

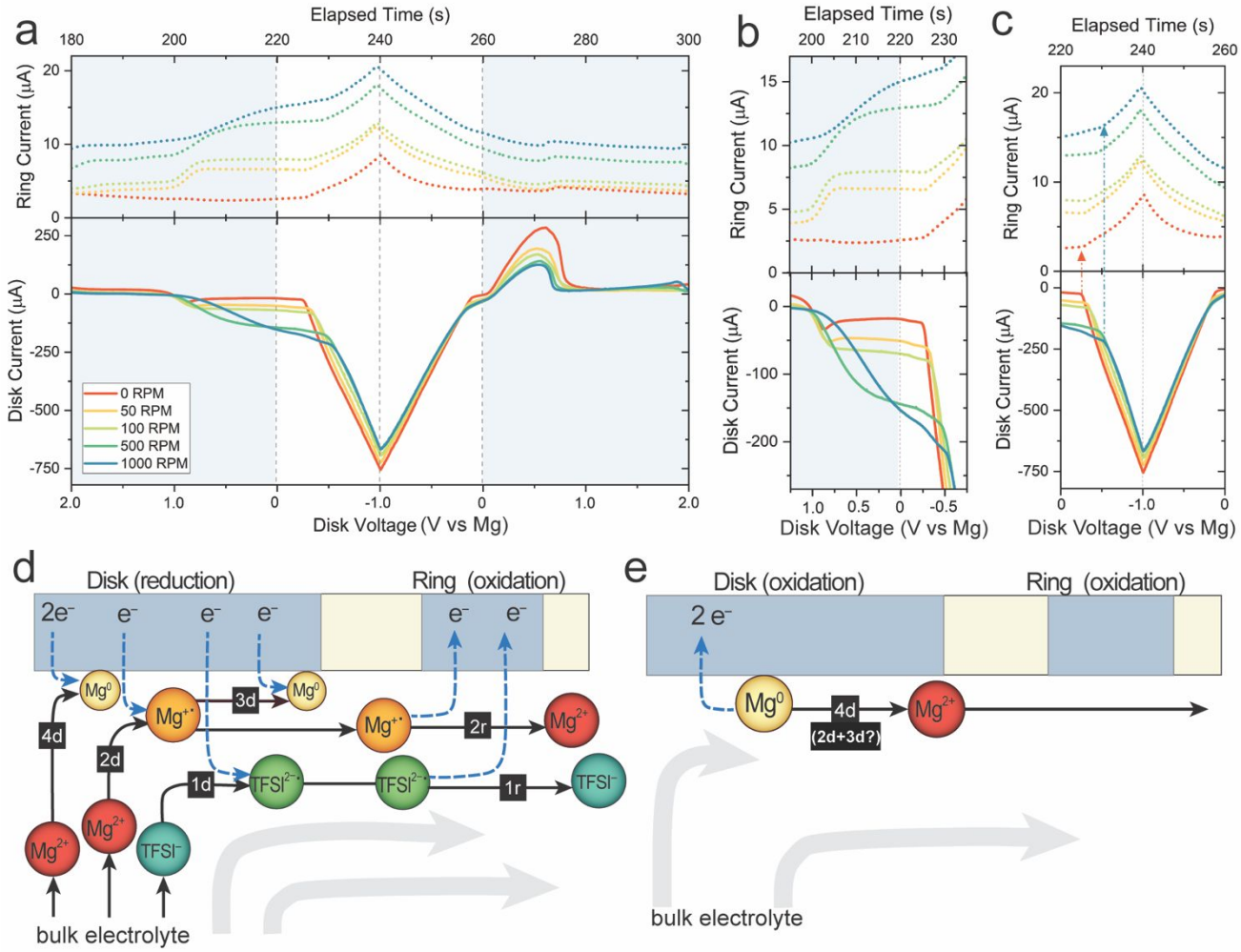

Figure 1. (a) RRDE of a CV cycle 0.4 M $Mg(TFSI)_2$ in 2.0 M DMA in THF at a disk electrode scan rate of 0.05 V/s between 2.2 V and -1.0 V with the ring electrode potential held at 2.0 V versus Mg. Dotted curves in the upper panel represent the ring current and solid curves in the lower panel represent disk current at rotation speeds of 0, 50, 100, 500, and 1000 RPM. Light blue shaded color blocks represent positive disk potential domains and unshaded blocks represent negative disk potential domains, dashed gray vertical reference lines indicate 0 V and the switching potential, -1.0 V for clarity. (b) Enlarged $TFSI^-$ redox region and (c) enlarged Mg redox region. RRDE schematics of possible reactions occurring (d) during reduction at the disk electrode (180 to 260 s) and (e) during oxidation at the disk electrode (>260 s).

A second set of reduction processes at the disk electrode were initiated at -0.4 V, corresponding to Mg^{2+} reduction (reactions $2d_{red}$, $3d_{red}$, and $4d_{red}$) with a maximum current of about -700 μA at -1.0 V (240 s), slightly decreasing with increased rotation speed, expanded in **Figure 1c**. The oxidation current at the ring (biased at 2.0 V) clearly indicates that one of the dominating Mg reduction reactions at the disk involves a sequential two-step, one-electron reaction (reactions $2d_{red}$ and $3d_{red}$) instead of a simple one-step, two electron reduction (reaction $4d_{red}$). Formation of the $Mg^{\bullet+}$-relevant radical at the disk is clearly indicated by the observation of a simultaneous ring current (8.44 μA at 0 RPM, 20.2 μA at 1000 RPM, reaction $2r_{ox}$). Therefore, during Mg^{2+} reduction, a partially solvated $Mg^{\bullet+}$-relevant radical intermediate is firstly formed (reaction $2d_{red}$), followed by oxidation to a Mg^{2+} species at the ring electrode (reaction $2r_{ox}$). To the best of our knowledge this is the first instance of an electrochemically captured $Mg^{\bullet+}$-relevant radical in solution. Ring current would be absent if Mg^{2+} underwent only a one-step, two-electron reduction from Mg^{2+} to Mg^0 ($4d_{red}$) that plates on the disk, as illustrated in **Figure 1d**. Additionally, literature reports that charge transfer may feasibly occur before complete desolvation of the Mg cation, supporting the appearance of the $Mg^{\bullet+}$-relevant radical species at the ring.[6,34,35] To further rule out possible contribution to the ring current from anions or solvents, control experiments of RRDE of a 0.4 M LiTFSI in THF and linear scan voltammetry of the solvent system (THF/DMA) (**Figure S4, S5)** were conducted where no obvious

ring current is observed at oxidation bias**.** It is worth noting that the Coulombic efficiency (CE%) in the RRDE experiments for both Mg electrolytes is overall lower than what has been previously reported in part because high rotation speed may remove loosely attached Mg deposits, but CE% is restored back once rotation is halted (**Figure S6**).

Experimentally probed electron transfer during Mg dissolution in *nh*Mg-DMA. As the disk potential was scanned back up into positive potentials (from 0 V to 2.2 V), two oxidation peaks were observed at about 0.5 V (270 s) and a very small one at 2.0 V (300 s) that correspond to Mg^0 oxidation, and possibly DMA degradation shown in **Figure 1a**. The disk current peak due to Mg^{2+} dissolution decreased with increasing rotation speed due to diminished formation of Mg^0 during plating at higher rotation speeds. The lack of corresponding current at the ring electrode indicated no obvious formation of $Mg^{\bullet+}$-relevant radicals. Therefore, the apparent dominating reaction at the disk is implied to effectively be a one-step, two-electron transfer reaction of Mg^0 to Mg^{2+} ($4d_{ox}$). A small perturbation of the ring current is visible (enlarged in **Figure S7**) that we hypothesize may be due to capacitive current changes due to anion migration near the ring, which is examined in greater depth in the APC electrolyte. The 2.0 M DMA in THF decomposition ($5d_{ox}$ may contribute to the elevated ring background) presented in **Figure S5,** showed an oxidative stability limit of ~2.25 V vs Mg. RRDE control experiments with the DMA-THF solvent (**Figure S8**) and the THF solvent (**Figure S9**) confirmed no solvent decomposition.

To briefly summarize the electron transfer mechanisms illustrated in **Figures 1d** and **1e**, four reduction reactions are proposed to possibly exist for *nh*Mg-DMA at the disk (200 – 260 s) including a reduction of the $TFSI^-$

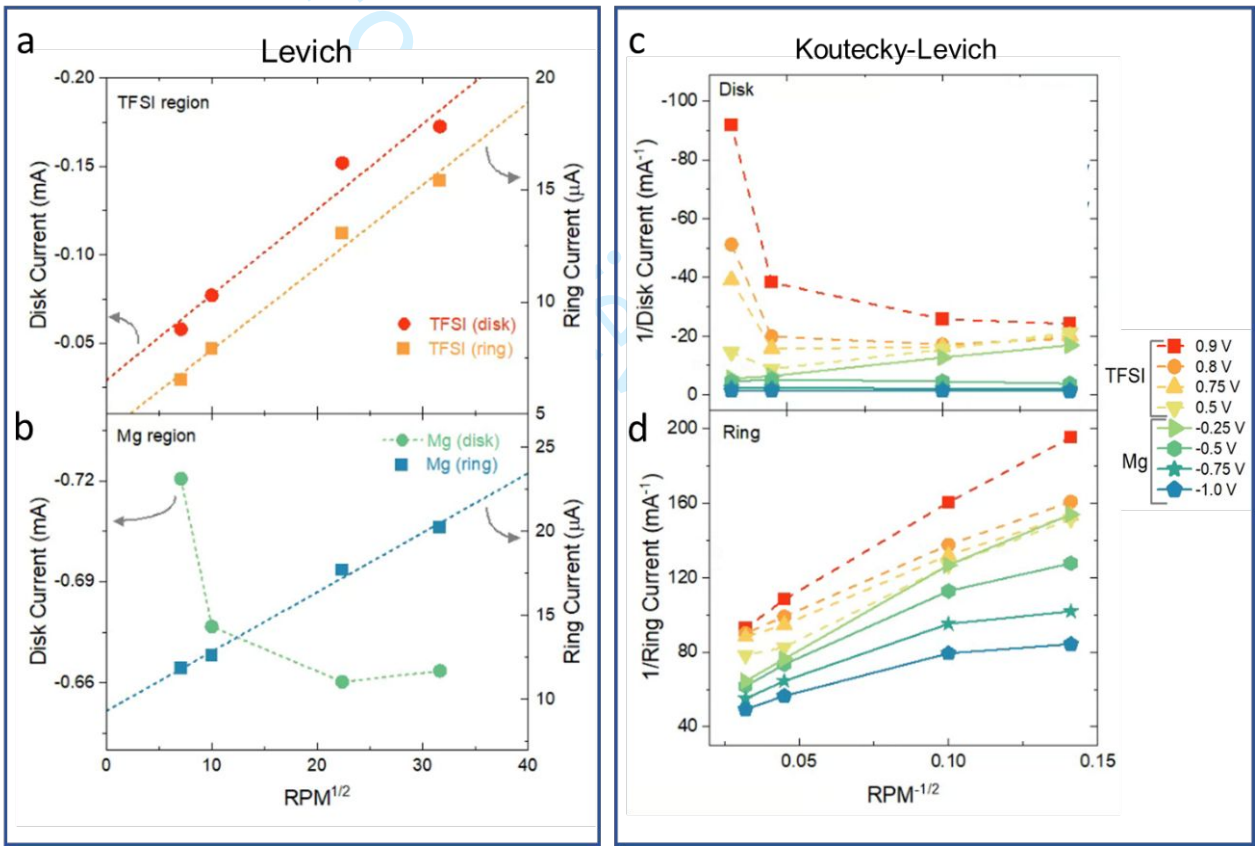

Figure 2. Levich plot of (a) the TFSI redox region at the disk and ring and (b) the Mg redox region at the disk and ring electrode and Koutecky-Levich plots of (c) disk current and (d) ring currents where dashed lines indicate TFSI redox regions and solid lines indicate Mg^{2+} redox regions in 0.4 M $Mg(TFSI)_2$ in 2.0 M DMA in THF.

anion ($1d_{red}$), a one-electron reduction of Mg^{2+} to $Mg^{\bullet+}$ ($2d_{red}$), a one-electron reduction of $Mg^{\bullet+}$ to Mg^0, ($3d_{red}$) and a two-electron reduction of Mg^{2+} to Mg^0 ($4d_{red}$). Two oxidation reactions are proposed at the disk electrode (260 – 300 s): oxidation of Mg^0 to Mg^{2+} ($4d_{ox}$) (or a facile two-step one-electron oxidation: $2d_{ox}$ and $3d_{ox}$) and the degrative

oxidation of dimethylamine ($5d_{ox}$). At the ring electrode there are two oxidation reactions proposed that include oxidation of the $TFSI^-$ anion or its reduction products ($1r_{ox}$), and the one-electron oxidation of $Mg^{\bullet+}$ to Mg^{2+} ($2r_{ox}$).

Mechanistic steps and qualitative kinetics in *nh*Mg-DMA. Rotation speeds of 0, 50, 100, 500, and 1000 RPM were applied to probe the reaction kinetics of the *nh*Mg-DMA electrolyte. The limiting currents from $TFSI^-$ reduction at the disk ($1d_{red}$), and oxidation at the ring electrode ($1r_{ox}$) in *nh*Mg-DMA roughly follow a linear Levich trend (**equation 1,** simulated in **Figure S10**) as shown in **Figure 2a**[29]. The Levich plot shows that the $TFSI^-$ redox reactions are influenced not only by the mass transport and diffusion but also possibly by the thermodynamics of desolvation, suggested by the non-zero intercept.[35,36] Koutecky Levich analysis in (**Figure 2c** and **2d**, dotted lines) revealed that the slope for the $TFSI^{\bullet 2-}$ oxidation reaction at the ring is not strongly potential dependent, suggesting the rate of electron transfer remains relatively rapid and unchanged. It is worth noting that at high rotation speed of >500 RPM a strong shift of the overpotential for $TFSI^-$ reduction at the disk causes a strongly non-linear segment in the Koutecky Levich data (**Figure 2c**). Results suggest that in both cases, the electron transfer process does not limit $TFSI^-$ redox reaction and that $TFSI^-$ reduction is partially reversible.

On the other hand, the Mg^{2+} reduction (reactions $2d_{red}$, $3d_{red}$, and $4d_{red}$) does *not* follow the expected Levich behavior for *nh*Mg-DMA in **Figure 2b**. Rather, an inverse Levich trend exists of decreased current with increased RPM, suggesting the occurrence of a twofold process. Reverse levich behavior has been previously reported for the electro-oxidation of glycerol and methanol systems where the premature removal of the reactants or partially reacted products is responsible for inhibited current at high rotation speeds.[37–39] Convection contributions at the disk electrode could similarly cause premature transport of Mg^{2+} species away from the electrode. Accordingly, either a slow adsorption step of Mg^{2+} species or a slow desolvation step is proposed to be a rate-limiting prerequisite

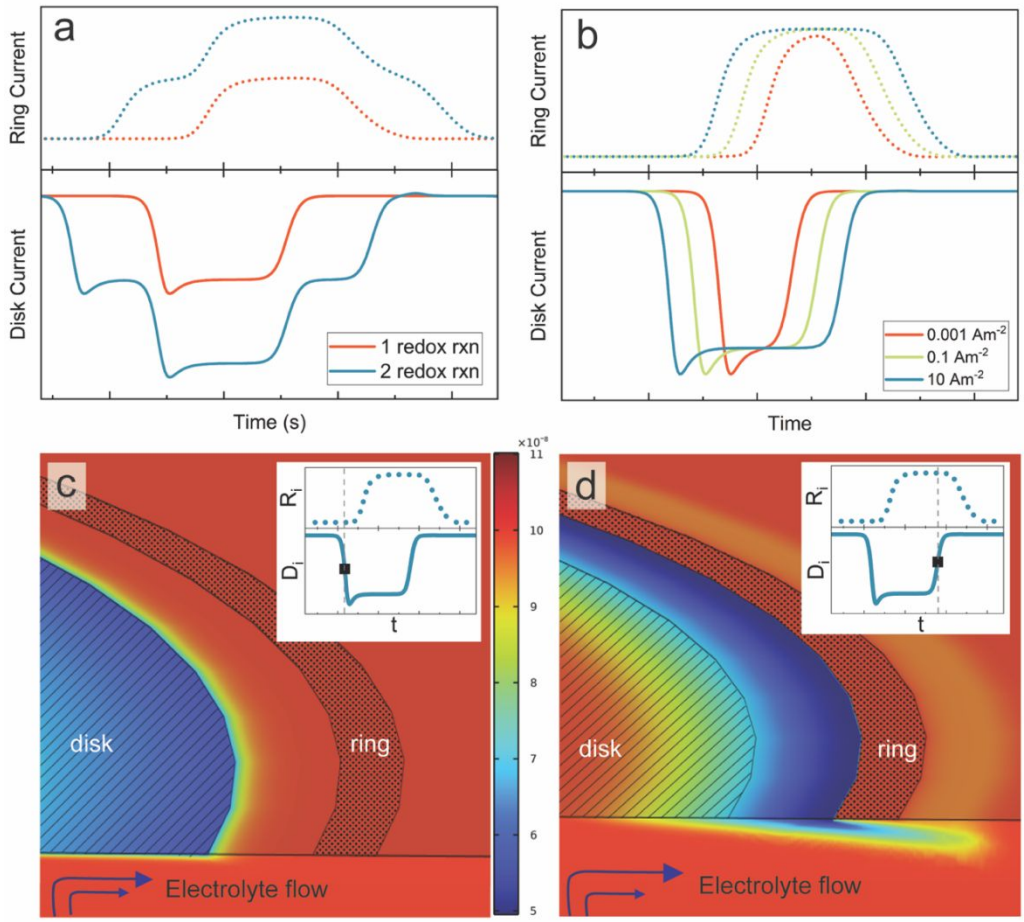

Figure 3. RRDE simulation of disk (lower panel, solid) and ring (upper panel, dotted) of (a) two independent reactions (blue) vs one reaction (red) representing coupled $TFSI^-$ and Mg^{2+} reductions and (b) the current response of a systems with exchange current densities of 0.001, 0.1, and 10 A/m^2. 2D simulation of Mg^{2+} concentration as (c) electrodeposition is initiated, corresponding to the black time point and reference line on the inset panel and (d) as reduction at the disk ceases at the black time point and reference line indicated on the inset panel.

before electron transfer, in agreement with reported literature of nonaqueous Mg electrolytes.[6,12,26,35,40–42] The slow desolvation of Mg^{2+} from an ion cluster of the *nh*Mg-DMA electrolyte slows the process of adsorption and greatly limits the deposition rate.[35] By contrast, however, the ring electrode current for $Mg^{\bullet+}$-relevant radical oxidation does follow the Levich relationship. Oxidation of $Mg^{\bullet+}$ radical at the ring electrode is thus not likely preceded by a slow chemical step. Neither reduction of Mg^{2+} nor oxidation of $Mg^{\bullet+}$-relevant radical reached diffusion limiting current plateaus, driven by a kinetically slow reaction process. Koutecky Levich analysis of Mg is shown as the solid curves in **Figures 2c** and **2d**. The Koutecky Levich equation assumes a reaction order of unity across the measurement, which may be inaccurate for Mg redox processes. The linear overpotential-dependent slope and y-intercept are additional indications of the existence of a second step attributed to adsorption and/or desolvation of Mg cations. This is in line with Treimer et al.'s work proposing **equation 8** as a modified Koutecky Levich equation that accounts for the existence of a reversible chemical step followed by a reversible electron transfer step mechanism (CE mechanism):

$$\frac{1}{i} = \frac{\mu}{nFADCK} + \left(\frac{[K+(1+K)e^{F\eta/RT}]}{0.201nFAD^{2/3}\nu^{-1/6}CK}\right)\omega^{-1/2} \qquad \text{(eq. 8)}$$

where μ is the reaction layer thickness; $K = {k_f}/{k_b}$, is the ratio of the forward and backward rate constants and η is the overpotential.[43] In **equation 8**, both the y-intercepts and slopes are found to be a function of applied potential which better agrees with Koutecky Levich behavior of both oxidation and reduction of Mg species. The decreasing Koutecky Levich slope implies that the rate of the forward reaction increases at each potential step resulting in the growth of the K term in **equation 8** due to the increased driving force. The apparent rate constants

(equivalent to the sum of the forward and backward rates) were calculated from the kinetic current derived from the Koutecky Levich intercepts, and was found to be more than three times higher: 2.1×10^{-7} m/s at -1 V versus 6.6×10^{-8} m/s at -0.5 V, consistent with a significant increase in k_f compared to k_b, which lead to an increase in K. The Koutecky Levich slope for the oxidation of $Mg^{\bullet+}$-relevant radical at the ring is evidently influenced by the electrode potential and consequently a CE mechanism is also proposed.

Chloride-based Mg Grignard electrolyte and Mg corrosion studies report the probable formation of intermediates that remain adsorbed at the electrode surface during Mg dissolution[12,41,44–46] which may provide an explanation as to why $Mg^{\bullet+}$-relevant radical was not observed at the ring during dissolution. With solely RRDE data, this is difficult to definitively resolve, but we postulate that the newly formed $Mg^{\bullet+}$-relevant radical may not yet be solvated, remaining close to the disk electrode, and rendering a second electron transfer more facile. Thus, a two-step, one-electron transfer reaction is still likely despite its absence in the disk and ring signals. The increase in Mg collection efficiency, N_c, (**Table S1**) with rotation speed is consistent with an unstable intermediate as the $Mg^{\bullet+}$ intermediate is expected to be a reactive species.[9,47] At higher rotation speeds, the travel time from disk to ring electrode decreases, resulting in the collection of a greater number of intermediate species at the ring.[29]

Coupled Butler-Volmer kinetics and Nernst-Planck simulation of faradic current. Butler-Volmer kinetics and Nernst-Planck were coupled with a mathematically defined solution flow pattern (equations 4-7) in COMSOL 6.1 to approximate a 2-D model of hydrodynamics in combination with electrochemistry at two independent electrodes (a ring and disk electrode) to further understand the current distribution contributed from one versus two redox reactions, and to investigate the influence of the hydrodynamic effect and the kinetics of the reaction rate on the current profile. The Nernst-Planck equation describes the three driving forces of ion flux including potential gradient, concentration gradient, and convection, all of which control the position and time-dependent concentration distribution, expressed and solved as partial differential equations. Concentration distribution from Nernst-Planck as the result of diffusion and convection was fed into Butler-Volmer kinetics. Currents calculated as an integration of flux at the disk electrode are shown in the lower panels with solid curves, and for the ring electrode shown in the upper panels with dotted curves.

Two scenarios were simulated in **Figure 3a**. (1) One reversible reduction reaction exists at the disk corresponding to Mg^{2+} to $Mg^{\bullet+}$ represented by the red curve ($2d_{red}$, $2r_{ox}$) and (2) two reversible reduction reactions corresponding to $TFSI^-$ to $TFSI^{\bullet 2-}$ ($1d_{red}$, $1r_{ox}$) and Mg^{2+} to $Mg^{\bullet+}$-relevant radical ($2d_{red}$, $2r_{ox}$) represented by the blue curve where the equilibrium redox potential of $TFSI^-$ is set to a voltage adequately higher than the Mg^{2+} equilibrium potential. **Figure 3a** shows that when only Mg^{2+} reduction is present, one limiting disk current plateau and one corresponding limiting ring current are visible. Upon the introduction of the $TFSI^-$ reaction at a higher potential, the reduction of $TFSI^-$ creates a shoulder on the original Mg^{2+} reduction current peak, and the two reactions occurring simultaneously both contribute to the overall current. The experimental data in **Figure 1a** clearly mirrors the two-reaction model supporting two simultaneous and independent reduction reactions at the disk and oxidation reactions at the ring where $TFSI^-$ reduction occurs at a higher potential (1.0 V vs Mg) than Mg^{2+} (< 0 V vs Mg).

The impact of reaction rate on the current profile was evaluated in **Figure 3b** by varying exchange current density (i_0). At the highest exchange current density, corresponding to a higher reaction rate, limiting current plateaus dominate the shape of the ring and disk curves. With decreasing exchange current density, the current plateau begins to diminish into a peak shape profile, implying that the slower reaction kinetics are responsible for creating a peak-shaped current signal instead of a typical limiting current sigmoid. In **Figure 1a**, the experimentally measured the $TFSI^-$ reduction / $TFSI^{\bullet 2-}$ oxidation shoulders achieved limiting current, but the Mg^{2+} reduction / $Mg^{\bullet+}$ oxidation does not, confirming our earlier conclusion of kinetically slow Mg redox reactions.

Figure 3c shows the simulated concentration distribution of Mg^{2+} at the start of Mg^{2+} reduction at the disk (time indicated in inset panel). As reduction begins, the concentration of Mg^{2+} at the disk electrode surface (area highlighted with stripes) rapidly depletes resulting in regions of low Mg^{2+} concentration, indicated by blue regions, also corresponding to regions of high $Mg^{\bullet+}$ concentration. Hydrodynamic forces drive the reduced $Mg^{\bullet+}$ species out radially towards the ring electrode (highlighted with dots). In **Figure 3d** (at the time indicated in inset) continuous reduction of Mg^{2+} at the disk electrode generated low concentrations of Mg^{2+} in the region between the ring and disk electrodes (i.e., high concentration of $Mg^{\bullet+}$), while the Mg^{2+} concentration at the ring electrode is initially equivalent to the bulk concentration. As the $Mg^{\bullet+}$-relevant radical species reaches the ring electrode, $Mg^{\bullet+}$ is converted back to Mg^{2+} as demonstrated by the sustained high Mg^{2+} concentration at the very surface of the ring

electrode. As in reality, the majority of the intermediate species is swept far enough away from the ring where it does not have an opportunity to react, determining the maximum collection efficiency.

Possible reactions in APC:

Reduction reactions at the disk electrode:

$Mg^{2+} + e^- \rightarrow Mg^{\bullet+}$ ($1d_{red}$)*

$Mg^{\bullet+} + e^- \rightarrow Mg^0$ ($2d_{red}$)*

$Mg^{2+} + 2e^- \rightarrow Mg^0$ ($3d_{red}$)

Oxidation reactions at the disk electrode:

$Mg^{\bullet+} - e^- \rightarrow Mg^{2+}$ ($1d_{ox}$)

$Mg^0 - e^- \rightarrow Mg^{\bullet+}$ ($2d_{ox}$)

$Mg^0 - 2e^- \rightarrow Mg^{2+}$ ($3d_{ox}$)*

Oxidation reactions at the ring:

$Mg^{\bullet+} - e^- \rightarrow Mg^{2+}$ ($1r_{ox}$)*

Experimentally probed electron transfer process of Mg deposition for APC electrolyte. Figure 4a shows the experimentally collected ring and disk currents of a 0.3 M APC electrolyte. APC is a well-studied electrolyte system with a variety of Mg species in solution including $MgCl^+$, $MgCl_2$, and $[Mg_2(\mu\text{-}Cl)_3 \cdot 6THF]^+$, the characteristic two octahedrally-coordinated Mg centers bridged with three Cl atoms and supported by six THF solvent molecules, commonly seen in most Grignard-derived Mg electrolytes.[11,15,18,21,48–51] Because of APC's contrasting solution structure compared to the $TFSI^-$-coordinated Mg in the *nh*Mg-DMA electrolyte, it is a good model system coupling to reveal the influence of the solution structure on the electron transfer mechanism.

In contrast to *nh*Mg-DMA, where an evident electrolyte reduction process occurs at 1.0 V before electrochemical deposition of Mg at -0.5 V, the APC system did not exhibit solvent or electrolyte reduction before Mg deposition. At -0.25 V, (235 s) the reduction current at the disk due to Mg reduction (possible reactions $1d_{red}$-$3d_{red}$) reached a maximum current of -1.1 mA, slightly decreasing in magnitude with rotation speed, expanded in

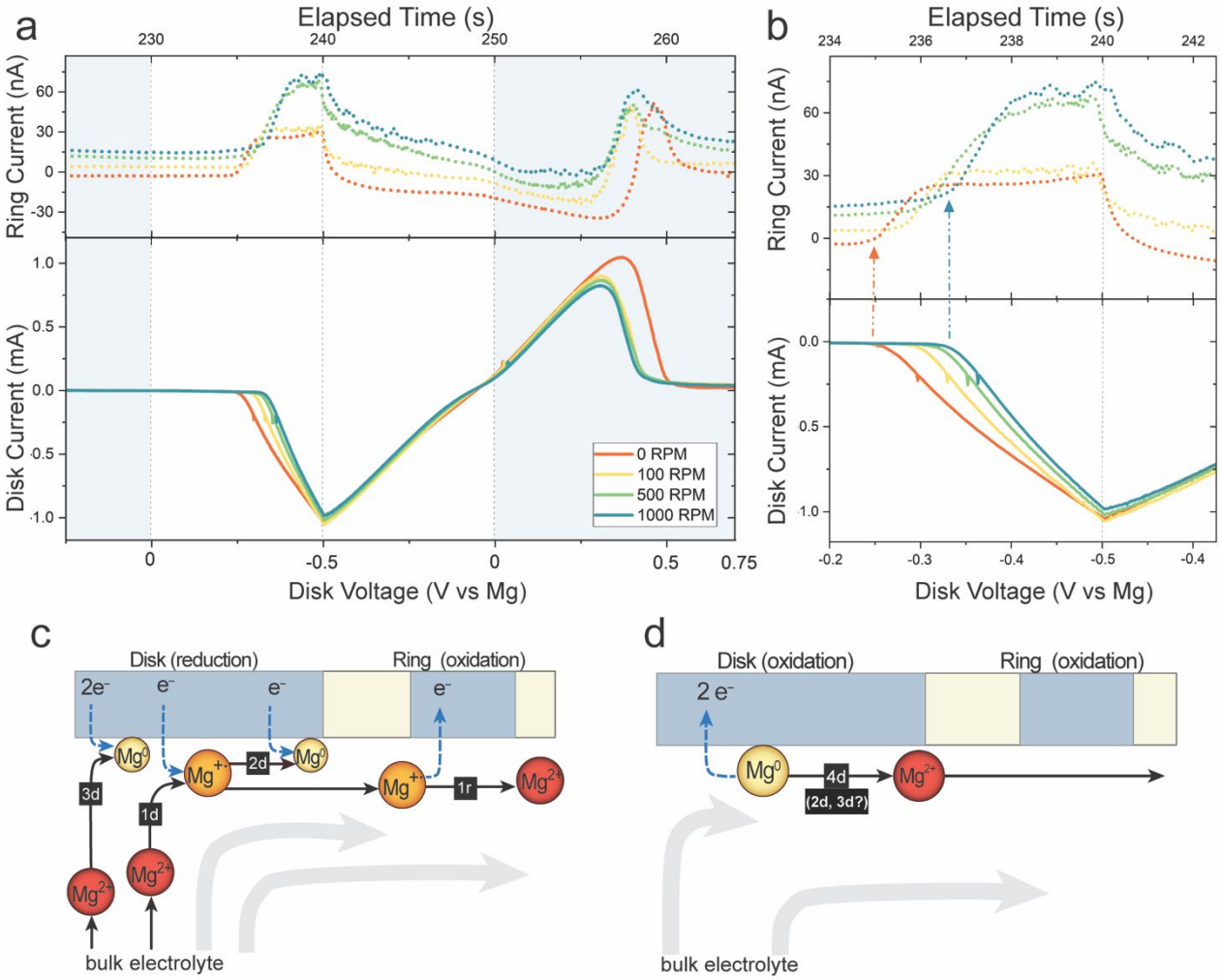

Figure 4. (a) RRDE CV cycle of 0.3 M APC between 0.75 V and -0.5 V at the disk electrode at a scan rate of 0.05 V/s and ring electrode biased at 0.75 V versus Mg. Upper panel with dotted curves represent the ring current and lower panel with solid curves represent disk current at rotation speeds of 0, 100, 500, and 1000 RPM. Light blue shaded color blocks represent positive disk potential domains and unshaded blocks represent negative disk potential domains, dashed gray vertical reference lines indicate 0 V and the switching potential, -0.5 V, for clarity. (b) Enlarged Mg redox region. RRDE schematics of reactions occurring (c) during reduction at the disk electrode (230 to 250 s) and (d) during oxidation at the disk electrode (>250 s).

Figure 4b. A Levich limiting ring current emerged concurrently with electrochemical deposition of Mg at the disk electrode during the cathodic scan, revealing the formation of the $Mg^{\bullet+}$-relevant radical at the disk and subsequent oxidation at the ring (reaction $1r_{ox}$). The limiting ring current magnitude increases with rotation speed-controlled mass transport, implying that the $Mg^{\bullet+}$-relevant radical has sufficiently fast electron transfer kinetics and obeys the Levich correlation. This finding is in complete contrast to the *nh*Mg-DMA system where slow kinetics inhibit the ring current from reaching a steady-state response, possibly as a side effect of the $TFSI^-$ evolved solvation structure. Another important finding is the product of the shorter transient time of the limiting current plateau due to rotation speed and its effect on the $Mg^{\bullet+}$-relevant radical. The decreased current ratio of i_{ring}/i_{disk} alludes to the stability of the intermediates. In addition, the ratios of i_{ring}/i_{disk} are three orders of magnitude smaller in APC than *nh*Mg-DMA suggesting the intermediate stability in APC is significantly lower than in *nh*Mg-DMA, demonstrated in **Table S1**. When the sweep direction was changed at -0.5 V (240 s) so the voltage of the disk electrode was scanned towards positive potentials, the $Mg^{\bullet+}$-relevant radical formation abruptly tapered off. The decreasing driving force evidently limits the formation of the $Mg^{\bullet+}$-relevant radical and the dominating reaction is an apparent one-step, two-electron process (reaction $3d_{red}$). It is unclear why this phenomenon is present in APC and absent in *nh*Mg-DMA.

Experimentally probed electron transfer process of Mg dissolution for APC electrolyte. A typical APC stripping curve of Mg^0 from the disk electrode was initiated at approximately 0 V (250 s) inducing a maximum oxidizing current of 1 mA at about 0.4 V at the disk (268 s, 0 RPM). Instead of a corresponding positive ring current indicating $Mg^{\bullet+}$-relevant radical, a negative current was observed. We hypothesize the negative current stems from changes in capacitive current due to the migration of anionic species from the ring to compensate for the positive charge density near the disk as Mg^0 is oxidized. A narrower stagnant layer migration corridor forms at higher RPM, explaining why high RPM experiences less negative current than low RPM. A ring current spike with subsequent stabilization of baseline current could either indicate the brief appearance of a $Mg^{\bullet+}$ intermediate, or more likely the sudden replenishment of anions and restoration of steady state capacitive current after plated Mg was depleted from the disk. A hint of this phenomena is also seen in *nh*Mg-DMA (**Figure S7**).

The processes of solvation and desolvation take a clear central role and lead to different steps preceding deposition and dissolution of Mg. During deposition where a desolvation process occurs, the first electron transfer likely takes place prior to full desolvation of the Mg^{2+} cation. With its remaining solvation shell, the $Mg^{\bullet+}$ can be transported to the ring for oxidation. During dissolution however, following the first electron transfer, the $Mg^{\bullet+}$-relevant radical is not immediately solvated. This creates the opportunity for a facile second electron transfer of the $Mg^{\bullet+}$ radical to form Mg^{2+} before solvation takes place, explaining the distinct absence of the $Mg^{\bullet+}$-relevant radical ring current in both *nh*Mg-DMA and APC during dissolution.

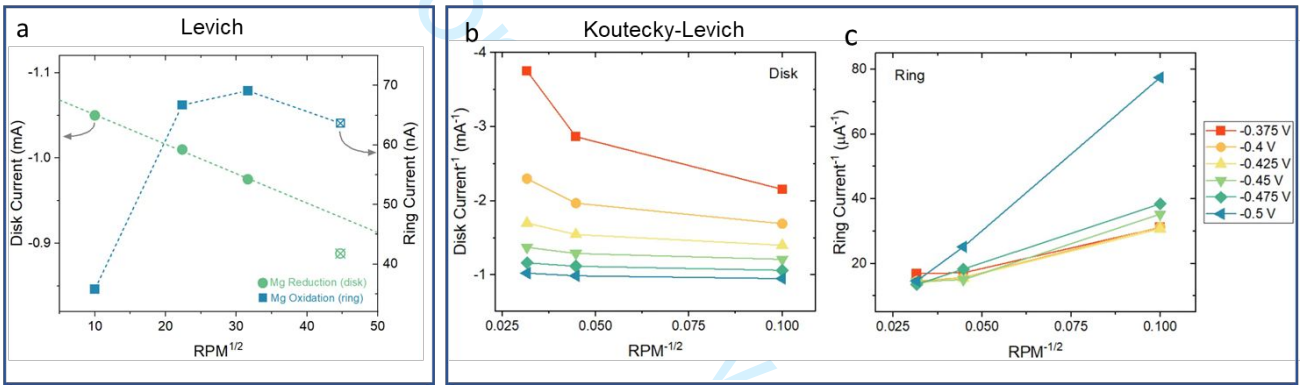

Figure 5. (a) Levich plot of the disk and ring electrode and Koutecky-Levich plots of (b) disk current and (c) ring current for 0.3 M APC electrolyte. A higher rotation speed of 2000 RPM is included in panel (a) for trend corroboration as a hollow data point, but it was not used in calculations due to uncertainty from turbulence.

Figure 4c shows the proposed reaction schematic during reduction reactions at the disk while **Figure 4d** shows a proposed reaction schematic during oxidation reactions at the disk. To conclude for APC, three primary reduction reactions are proposed to occur at the disk including reduction of Mg^{2+} to $Mg^{\bullet+}$ in a one-electron reaction ($1d_{red}$), reduction of $Mg^{\bullet+}$ to Mg^0 in another one-electron transfer reaction ($2d_{red}$), and possibly reduction of Mg^{2+} to Mg^0 in a two-electron transfer ($3d_{red}$). Three oxidation reactions are proposed at the disk after 250 s including oxidation of $Mg^{\bullet+}$ to Mg^{2+} in a one-electron reaction ($1d_{ox}$), oxidation of Mg^0 to $Mg^{\bullet+}$ in a one-electron reaction ($2d_{ox}$), and a possible oxidation of Mg^0 to Mg^{2+} in a two-electron reaction ($3d_{ox}$). The only major redox reaction proposed at the ring is a single electron oxidation of $Mg^{\bullet+}$ to Mg^{2+} ($1r_{ox}$).

Mechanistic steps and qualitative kinetics in APC. Levich plots of disk and ring shown in **Figure 5a** of 0.3M APC at 100, 500, and 1000 RPM show contrasting disk and ring behavior where the reduction of Mg^{2+} at the disk shows reversed Levich trend and oxidation of $Mg^{\bullet+}$ at the ring follows the Levich equation correlation, akin to *nh*Mg-DMA. The reverse Levich behavior at the disk is attributed to an adsorption or slow desolvation step for Mg^{2+} reduction, where increased convection leads to premature transport of Mg^{2+} species away from the disk. An adsorption step agrees with Aurbach's and others' work studying the APC electrolyte and electrodeposition of Mg.[3,41,52,53] A report from Viestfrid et al. specifically proposed that the potential-dependent adsorption of $MgCl^+$ can become the rate determining step at high overpotentials, and the reduction of Mg^{2+} to $Mg^{\bullet+}$-relevant radical (a

neutral $MgCl^{\bullet}$ species) would be kinetically slow, contributing to the overall sluggishness of the first reduction step.[27] The Levich plots also demonstrate activation energy-controlled thermodynamics of desolvation with non-zero intercepts.[36]

Koutecky Levich studies of the disk electrode and ring electrode during electrodeposition are presented in **Figures 5b** and **5c**. At both the disk and the ring electrode the change in Koutecky Levich slope further supports a chemical adsorption step before electron transfer occurs described by a modified Koutecky Levich equation (**equation 8**). The CE mechanism at the disk proceeds via a slow adsorption/desolvation of a Mg^{2+} species, such as $MgCl^{+}$, to the disk electrode before a first electron transfer reaction occurs leading to formation of a partially solvated $Mg^{\bullet+}$-relevant radical. If the $Mg^{\bullet+}$-relevant radical further desolvates, and remains close to the disk, a second electron transfer results in plated Mg^0 metal.

Electron transfer mechanisms in different solvation environments. Remarkably, two key mechanistic steps of electron transfer of Mg in APC and *nh*Mg-DMA electrolyte appear to be very similar, despite the drastic differences in solution structure: (1) both exhibited the formation of a $Mg^{\bullet+}$ intermediate during the reduction of Mg^{2+}, directly experimentally verifying that the Mg^{2+} reduction pathway involves two discrete electron transfer steps; (2) both were victim to sluggish preceding adsorption or dissolution steps of Mg^{2+} on the disk electrode before electron transfer, evidenced by the reverse Levich behavior and Koutecky Levich potential-dependent slopes of Mg^{2+} reduction. In both electrolytes, initial desolvation or adsorption of Mg^{2+} at the disk during deposition is clearly a critical rate-limiting step before electron transfer and is noticeably impeded by enhanced mass transport.

A major difference between the two electrolyte systems is the achievement of a limiting current for the oxidation of $Mg^{\bullet+}$-relevant radical in APC, clearly the most facile reaction proposed here. In further support of that, the *nh*Mg-DMA ring vs disk current ratio was three orders of magnitude larger than APC, due either to the faster $Mg^{\bullet+}$-relevant radical kinetics of APC that lead to a second electron transfer at the disk or reduced intermediate stability compared to *nh*Mg-DMA. Another important difference supporting faster APC kinetics is that *nh*Mg-DMA reactions are more heavily impacted by the rotation speed due to a kinetically slower Mg^{2+} reduction process. Minor differences stem from degree of cation solvation. In *nh*Mg-DMA, the absence of the $Mg^{\bullet+}$-relevant radical at the ring during Mg^0 dissolution at the disk is likely due to not-yet-solvated $Mg^{\bullet+}$-relevant species, allowing a facile second electron transfer step to occur before solvation. In APC, dissolution of Mg at the disk results in a negative ring current followed by a quick positive current spike. Such unusual negative current may be attributed to the migration of anions at the ring electrode surface towards the newly formed Mg cations at the disk and the current spike attributed to capacitive current due to anion replenishment at the ring electrode instead of $Mg^{\bullet+}$-relevant radical formation. While at first seemingly different between *nh*Mg-DMA and APC, the main implication is the same: there is no detected $Mg^{\bullet+}$ at the ring during electrochemical dissolution at the disk. Reduction of $TFSI^-$ contributes a noticeable limiting current shoulder before Mg^{2+} reduction resulting from significant ion pairing of $TFSI^-$ and Mg^{2+} in solution.

CONCLUSIONS

Work here has clarified aspects of the electron transfer and mass transport mechanisms of reversible Mg deposition in both a $Mg(TFSI)_2$ in THF/DMA electrolyte and a traditional APC electrolyte. It was discovered that the two systems exhibit strikingly similar CE mechanisms for the Mg cation in which a chemical step, characterized as an adsorption or dissolution/solvation step, precedes two discrete electron transfers despite large discrepancies in the Mg^{2+} cation's coordination environment. These results suggest that (1) the mechanism of electrochemical deposition and dissolution of the Mg cation in non-aqueous electrolytes appear to be common across chloride and $TFSI^-$ solvation environments, and (2) differences in electrochemistry and kinetics seem dependent predominantly on solvent and anion electrochemistry. Having a deeper understanding of the fundamental mechanism of Mg redox chemistry will enable intentional and informed design of the next generation of nonaqueous Mg electrolyte candidates for rechargeable battery chemistries.

ASSOCIATED CONTENT

Supporting Information

The Supporting Information is available free of charge on the ACS Publications website. Cycled electrolyte FTIR, Levich simulation, RRDE of early cycles, COMSOL simulation geometry

AUTHOR INFORMATION

Corresponding Author

Niya Sa – *Department of Chemistry, University of Massachusetts Boston, Boston, Massachusetts 02125, United States*
Email: Niya.Sa@umb.edu

Authors

Genevieve Asselin – *Department of Chemistry, University of Massachusetts Boston, Boston, Massachusetts 02125, United States*

Zicheng Yang – *Department of Chemistry, University of Massachusetts Boston, Boston, Massachusetts 02125, United States*

Notes

The authors declare no competing financial interests.

ACKNOWLEDGMENT

This work is financially supported by the National Science Foundation (NSF), the NSF CAREER grant (no. 2047753). The NSF Center for Interfacial Ionics (grant no. 2221599) sponsored by the Centers for Chemical Innovation (CCI) Program in the Division of Chemistry is acknowledged for supporting the Mg interface ion transfer kinetic data analysis. Leslie Gates and Olivia Paden are acknowledged to help performing control experiments presented in SI. Author Genevieve Asselin is financially sponsored by the U.S. Department of Energy, Office of Science, Office of Workforce Development for Teachers and Scientists, Office of Science Graduate Student Research (SCGSR) program and the CSM Doctoral Fellowship (UMass). The SCGSR program is administered by the Oak Ridge Institute for Science and Education (ORISE) for the DOE. ORISE is managed by ORAU under contract number DE-SC0014664. All opinions expressed in this paper are the author's and do not necessarily reflect the policies and views of DOE, ORAU, or ORISE. The Proposal Development Grant from the University of Massachusetts Boston is acknowledged.

REFERENCES

(1) Muldoon, J.; Bucur, C. B.; Gregory, T. Quest for Nonaqueous Multivalent Secondary Batteries: Magnesium and Beyond. *Chem. Rev.* **2014**, *114* (23), 11683–1172010.1021/cr500049y.

(2) Deivanayagam, R.; Ingram, B. J.; Shahbazian-Yassar, R. Progress in Development of Electrolytes for Magnesium Batteries. *Energy Storage Mater.* **2019**, *21* (April), 136–15310.1016/j.ensm.2019.05.028.

(3) Yoo, H. D.; Shterenberg, I.; Gofer, Y.; Gershinsky, G.; Pour, N.; Aurbach, D. Mg Rechargeable Batteries: An on-Going Challenge. *Energy Environ. Sci.* **2013**, *6* (8), 226510.1039/c3ee40871j.

(4) Aurbach, D.; Lu, Z.; Schechter, A.; Gofer, Y.; Gizbar, H.; Turgeman, R.; Cohen, Y.; Moshkovich, M.; Levi, E. Prototype Systems for Rechargeable Magnesium Batteries. *Nature* **2000**, *407* (6805), 724–72710.1038/35037553.

(5) Ponrouch, A.; Bitenc, J.; Dominko, R.; Lindahl, N.; Johansson, P.; Palacin, M. R. Multivalent Rechargeable Batteries. *Energy Storage Mater.* **2019**, *20* (February), 253–26210.1016/j.ensm.2019.04.012.

(6) Forero-Saboya, J. D.; Tchitchekova, D. S.; Johansson, P.; Palacín, M. R.; Ponrouch, A. Interfaces and Interphases in Ca and Mg Batteries. *Adv. Mater. Interfaces* **2022**, *9* (8), 210157810.1002/admi.202101578.

(7) Zhang, Q.-H.; Liu, P.; Zhu, Z.-J.; Li, X.-R.; Zhang, J.-Q.; Cao, F.-H. Electrochemical Detection of Univalent Mg Cation: A Possible Explanation for the Negative Difference Effect during Mg Anodic Dissolution. *J. Electroanal. Chem.* **2021**, *880*, 11483710.1016/j.jelechem.2020.114837.

(8) Bonyhady, S. J.; Green, S. P.; Jones, C.; Nembenna, S.; Stasch, A. A Dimeric Magnesium(I) Compound as a Facile Two-Center/Two-Electron Reductant. *Angew. Chemie Int. Ed.* **2009**, *48* (16), 2973–297710.1002/anie.200900331.

(9) Rajput, N. N.; Qu, X.; Sa, N.; Burrell, A. K.; Persson, K. A. The Coupling between Stability and Ion Pair Formation in Magnesium Electrolytes from First-Principles Quantum Mechanics and Classical Molecular Dynamics. *J. Am. Chem. Soc.* **2015**, *137* (9), 3411–342010.1021/jacs.5b01004.

(10) Baskin, A.; Prendergast, D. Exploration of the Detailed Conditions for Reductive Stability of Mg(TFSI) 2 in Diglyme: Implications for Multivalent Electrolytes. *J. Phys. Chem. C* **2016**, *120* (7), 3583–359410.1021/acs.jpcc.5b08999.

(11) Ta, K.; See, K. A.; Gewirth, A. A. Elucidating Zn and Mg Electrodeposition Mechanisms in Nonaqueous Electrolytes for Next-Generation Metal Batteries. *J. Phys. Chem. C* **2018**, *122* (25), 13790–1379610.1021/acs.jpcc.8b00835.

(12) Ha, Y.; Zeng, Z.; Barile, C. J.; Chang, J.; Nuzzo, R. G.; Greeley, J.; Gewirth, A. A. Dynamic Surface Stress Response during Reversible Mg Electrodeposition and Stripping. *J. Electrochem. Soc.* **2016**, *163* (13), A2679–A268410.1149/2.0721613jes.

(13) Aurbach, D.; Suresh, G. S.; Levi, E.; Mitelman, A.; Mizrahi, O.; Chusid, O.; Brunelli, M. Progress in Rechargeable Magnesium Battery Technology. *Adv. Mater.* **2007**, *19* (23), 4260–426710.1002/adma.200701495.

(14) Tutusaus, O.; Mohtadi, R.; Arthur, T. S.; Mizuno, F.; Nelson, E. G.; Sevryugina, Y. V. An Efficient Halogen-Free Electrolyte for Use in Rechargeable Magnesium Batteries. *Angew. Chemie Int. Ed.* **2015**, *54* (27), 7900–790410.1002/anie.201412202.

(15) Muldoon, J.; Bucur, C. B.; Oliver, A. G.; Sugimoto, T.; Matsui, M.; Kim, H. S.; Allred, G. D.; Zajicek, J.; Kotani, Y. Electrolyte Roadblocks to a Magnesium Rechargeable Battery. *Energy Environ. Sci.* **2012**, *5* (3), 594110.1039/c2ee03029b.

(16) Sa, N.; Rajput, N. N.; Wang, H.; Key, B.; Ferrandon, M.; Srinivasan, V.; Persson, K. A.; Burrell, A. K.; Vaughey, J. T. Concentration Dependent Electrochemical Properties and Structural Analysis of a Simple Magnesium Electrolyte: Magnesium Bis(Trifluoromethane Sulfonyl)Imide in Diglyme. *RSC Adv.* **2016**, *6* (114), 113663–11367010.1039/C6RA22816J.

(17) Fan, S.; Asselin, G. M.; Pan, B.; Wang, H.; Ren, Y.; Vaughey, J. T.; Sa, N. A Simple Halogen-Free Magnesium Electrolyte for Reversible Magnesium Deposition through Cosolvent Assistance. *ACS Appl. Mater. Interfaces* **2020**, *12* (9), 10252–1026010.1021/acsami.9b18833.

(18) Rajput, N. N.; Seguin, T. J.; Wood, B. M.; Qu, X.; Persson, K. A. Elucidating Solvation Structures for Rational Design of Multivalent Electrolytes—A Review. *Top. Curr. Chem.* **2018**, *376* (3), 1910.1007/s41061-018-0195-2.

(19) Sa, N.; Kinnibrugh, T. L.; Wang, H.; Sai Gautam, G.; Chapman, K. W.; Vaughey, J. T.; Key, B.; Fister, T. T.; Freeland, J. W.; Proffit, D. L.; Chupas, P. J.; Ceder, G.; Bareno, J. G.; Bloom, I. D.; Burrell, A. K. Structural Evolution of Reversible Mg Insertion into a Bilayer Structure of V2O5 · n H2O Xerogel Material. *Chem. Mater.* **2016**, *28* (9), 2962–296910.1021/acs.chemmater.6b00026.

(20) Fan, S.; Cora, S.; Sa, N. Evolution of the Dynamic Solid Electrolyte Interphase in Mg Electrolytes for Rechargeable Mg-Ion Batteries. *ACS Appl. Mater. Interfaces* **2022**, *14* (41), 46635–4664510.1021/acsami.2c13037.

(21) Canepa, P.; Jayaraman, S.; Cheng, L.; Rajput, N. N.; Richards, W. D.; Gautam, G. S.; Curtiss, L. A.; Persson, K. A.; Ceder, G. Elucidating the Structure of the Magnesium Aluminum Chloride Complex Electrolyte for Magnesium-Ion Batteries. *Energy Environ. Sci.* **2015**, *8* (12), 3718–373010.1039/C5EE02340H.

(22) Lapidus, S. H.; Rajput, N. N.; Qu, X.; Chapman, K. W.; Persson, K. A.; Chupas, P. J. Solvation Structure and Energetics of Electrolytes for Multivalent Energy Storage. *Phys. Chem. Chem. Phys.* **2014**, *16* (40), 21941–2194510.1039/C4CP03015J.

(23) Nie, M.; Abraham, D. P.; Seo, D. M.; Chen, Y.; Bose, A.; Lucht, B. L. Role of Solution Structure in Solid Electrolyte Interphase Formation on Graphite with LiPF 6 in Propylene Carbonate. *J. Phys. Chem. C* **2013**, *117* (48), 25381–2538910.1021/jp409765w.

(24) Liu, T.; Shao, Y.; Li, G.; Gu, M.; Hu, J.; Xu, S.; Nie, Z.; Chen, X.; Wang, C.; Liu, J. A Facile Approach Using MgCl2 to Formulate High Performance Mg2+ Electrolytes for Rechargeable Mg Batteries. *J. Mater. Chem. A* **2014**, *2* (10), 343010.1039/c3ta14825d.

(25) Armand, M.; Tarascon, J. M. Building Better Batteries. *Nature* **2008**, *451* (7), 652–657.

(26) Benmayza, A.; Ramanathan, M.; Arthur, T. S.; Matsui, M.; Mizuno, F.; Guo, J.; Glans, P.-A.; Prakash, J. Effect of Electrolytic Properties of a Magnesium Organohaloaluminate Electrolyte on Magnesium Deposition. *J. Phys. Chem. C* **2013**, *117* (51), 26881–2688810.1021/jp4077068.

(27) Viestfrid, Y.; Levi, M. D.; Gofer, Y.; Aurbach, D. Microelectrode Studies of Reversible Mg Deposition in

THF Solutions Containing Complexes of Alkylaluminum Chlorides and Dialkylmagnesium. *J. Electroanal. Chem.* **2005**, *576* (2), 183–19510.1016/j.jelechem.2004.09.034.

(28) Aurbach, D.; Schechter, A.; Moshkovich, M.; Cohen, Y. On the Mechanisms of Reversible Magnesium Deposition Processes. *J. Electrochem. Soc.* **2001**, *148* (9), A100410.1149/1.1387980.

(29) Bard, A. J.; Faulkner, L. R. *Electrochemical Methods - Fundamentals and Applications*, 2nd ed.; John Wiley & Sons, 2001.

(30) Connell, J. G.; Zorko, M.; Agarwal, G.; Yang, M.; Liao, C.; Assary, R. S.; Strmcnik, D.; Markovic, N. M. Anion Association Strength as a Unifying Descriptor for the Reversibility of Divalent Metal Deposition in Nonaqueous Electrolytes. *ACS Appl. Mater. Interfaces* **2020**, *12* (32), 36137–3614710.1021/acsami.0c09404.

(31) Alwast, D.; Schnaidt, J.; Hancock, K.; Yetis, G.; Behm, R. J. Effect of Li + and Mg 2+ on the Electrochemical Decomposition of the Ionic Liquid 1-Butyl-1- Methylpyrrolidinium Bis(Trifluoromethanesulfonyl)Imide and Related Electrolytes. *ChemElectroChem* **2019**, *6* (12), 3009–301910.1002/celc.201900371.

(32) Yildirim, H.; Haskins, J. B.; Bauschlicher, C. W.; Lawson, J. W. Decomposition of Ionic Liquids at Lithium Interfaces. 1. Ab Initio Molecular Dynamics Simulations. *J. Phys. Chem. C* **2017**, *121* (51), 28214–2823410.1021/acs.jpcc.7b09657.

(33) Han, J.; Zheng, Y.; Guo, N.; Balbuena, P. B. Calculated Reduction Potentials of Electrolyte Species in Lithium–Sulfur Batteries. *J. Phys. Chem. C* **2020**, *124* (38), 20654–2067010.1021/acs.jpcc.0c04173.

(34) Attias, R.; Dlugatch, B.; Chae, M. S.; Goffer, Y.; Aurbach, D. Changes in the Interfacial Charge-Transfer Resistance of Mg Metal Electrodes, Measured by Dynamic Electrochemical Impedance Spectroscopy. *Electrochem. commun.* **2021**, *124*, 10695210.1016/j.elecom.2021.106952.

(35) Drews, J.; Jankowski, P.; Häcker, J.; Li, Z.; Danner, T.; García Lastra, J. M.; Vegge, T.; Wagner, N.; Friedrich, K. A.; Zhao-Karger, Z.; Fichtner, M.; Latz, A. Modeling of Electron-Transfer Kinetics in Magnesium Electrolytes: Influence of the Solvent on the Battery Performance. *ChemSusChem* **2021**, *14* (21), 4820–483510.1002/cssc.202101498.

(36) Clarke, C. J.; Browning, G. J.; Donne, S. W. An RDE and RRDE Study into the Electrodeposition of Manganese Dioxide. *Electrochim. Acta* **2006**, *51* (26), 5773–578410.1016/j.electacta.2006.03.013.

(37) Melle, G. B.; Machado, E. G.; Mascaro, L. H.; Sitta, E. Effect of Mass Transport on the Glycerol Electro-Oxidation. *Electrochim. Acta* **2019**, *296*, 972–97910.1016/j.electacta.2018.11.085.

(38) Puthiyapura, V. K.; Lin, W.-F.; Russell, A. E.; Brett, D. J. L.; Hardacre, C. Effect of Mass Transport on the Electrochemical Oxidation of Alcohols Over Electrodeposited Film and Carbon-Supported Pt Electrodes. *Top. Catal.* **2018**, *61* (3–4), 240–25310.1007/s11244-018-0893-6.

(39) Zülke, A.; Perroni, P.; Machado, E. G.; Varela, H. Rrde Studies of Glycerol Electro-Oxidation: Local PH Variation and Oscillatory Dynamics. *ECS Trans.* **2017**, *77* (11), 1643–165010.1149/07711.1643ecst.

(40) Wang, H.; Feng, X.; Chen, Y.; Liu, Y.-S.; Han, K. S.; Zhou, M.; Engelhard, M. H.; Murugesan, V.; Assary, R. S.; Liu, T. L.; Henderson, W.; Nie, Z.; Gu, M.; Xiao, J.; Wang, C.; Persson, K.; Mei, D.; Zhang, J.-G.; Mueller, K. T.; Guo, J.; Zavadil, K.; Shao, Y.; Liu, J. Reversible Electrochemical Interface of Mg Metal and Conventional Electrolyte Enabled by Intermediate Adsorption. *ACS Energy Lett.* **2020**, *5* (1), 200–20610.1021/acsenergylett.9b02211.

(41) Mizuno, F.; Singh, N.; Arthur, T. S.; Fanson, P. T.; Ramanathan, M.; Benmayza, A.; Prakash, J.; Liu, Y. S.; Glans, P. A.; Guo, J. Understanding and Overcoming the Challenges Posed by Electrode/Electrolyte Interfaces in Rechargeable Magnesium Batteries. *Front. Energy Res.* **2014**, *2* (NOV), 1–1110.3389/fenrg.2014.00046.

(42) Ye, Y.; Wu, C. H.; Zhang, L.; Liu, Y.-S.; Glans-Suzuki, P.-A.; Guo, J. Using Soft X-Ray Absorption Spectroscopy to Characterize Electrode/Electrolyte Interfaces in-Situ and Operando. *J. Electron Spectros. Relat. Phenomena* **2017**, *221*, 2–910.1016/j.elspec.2017.05.002.

(43) Treimer, S.; Tang, A.; Johnson, D. C. A Consideration of the Application of Koutecký-Levich Plots in the Diagnoses of Charge-Transfer Mechanisms at Rotated Disk Electrodes. *Electroanalysis* **2002**, *14* (3), 16510.1002/1521-4109(200202)14:3<165::AID-ELAN165>3.0.CO;2-6.

(44) Baril, G.; Galicia, G.; Deslouis, C.; Pébère, N.; Tribollet, B.; Vivier, V. An Impedance Investigation of the Mechanism of Pure Magnesium Corrosion in Sodium Sulfate Solutions. *J. Electrochem. Soc.* **2007**, *154* (2),

C10810.1149/1.2401056.
(45) Gomes, M. P.; Costa, I.; Pébère, N.; Rossi, J. L.; Tribollet, B.; Vivier, V. On the Corrosion Mechanism of Mg Investigated by Electrochemical Impedance Spectroscopy. *Electrochim. Acta* **2019**, *306*, 61–7010.1016/j.electacta.2019.03.080.
(46) Huang, J.; Song, G.-L.; Atrens, A.; Dargusch, M. What Activates the Mg Surface—A Comparison of Mg Dissolution Mechanisms. *J. Mater. Sci. Technol.* **2020**, *57*, 204–22010.1016/j.jmst.2020.03.060.
(47) Qu, X.; Zhang, Y.; Rajput, N. N.; Jain, A.; Maginn, E.; Persson, K. A. Computational Design of New Magnesium Electrolytes with Improved Properties. *J. Phys. Chem. C* **2017**, *121* (30), 16126–1613610.1021/acs.jpcc.7b04516.
(48) Mizrahi, O.; Amir, N.; Pollak, E.; Chusid, O.; Marks, V.; Gottlieb, H.; Larush, L.; Zinigrad, E.; Aurbach, D. Electrolyte Solutions with a Wide Electrochemical Window for Rechargeable Magnesium Batteries. *J. Electrochem. Soc.* **2008**, *155* (2), A10310.1149/1.2806175.
(49) Barile, C. J.; Barile, E. C.; Zavadil, K. R.; Nuzzo, R. G.; Gewirth, A. A. Electrolytic Conditioning of a Magnesium Aluminum Chloride Complex for Reversible Magnesium Deposition. *J. Phys. Chem. C* **2014**, *118* (48), 27623–2763010.1021/jp506951b.
(50) See, K. A.; Chapman, K. W.; Zhu, L.; Wiaderek, K. M.; Borkiewicz, O. J.; Barile, C. J.; Chupas, P. J.; Gewirth, A. A. The Interplay of Al and Mg Speciation in Advanced Mg Battery Electrolyte Solutions. *J. Am. Chem. Soc.* **2016**, *138* (1), 328–33710.1021/jacs.5b10987.
(51) See, K. A.; Liu, Y. M.; Ha, Y.; Barile, C. J.; Gewirth, A. A. Effect of Concentration on the Electrochemistry and Speciation of the Magnesium Aluminum Chloride Complex Electrolyte Solution. *ACS Appl. Mater. Interfaces* **2017**, *9* (41), 35729–3573910.1021/acsami.7b08088.
(52) Aurbach, D.; Turgeman, R.; Chusid, O.; Gofer, Y. Spectroelectrochemical Studies of Magnesium Deposition by in Situ FTIR Spectroscopy. *Electrochem. commun.* **2001**, *3* (5), 252–26110.1016/S1388-2481(01)00148-5.
(53) Canepa, P.; Gautam, G. S.; Malik, R.; Jayaraman, S.; Rong, Z.; Zavadil, K. R.; Persson, K.; Ceder, G. Understanding the Initial Stages of Reversible Mg Deposition and Stripping in Inorganic Non-Aqueous Electrolytes. *Chem. Mater.* **2015**, *27* (9), 3317–332510.1021/acs.chemmater.5b00389.

1